The Astrophysical Journal Letters, 907:L36 (14pp), 2021 February 1 https://doi.org/10.3847/2041-8213/abd9b8

A Heavy Molecular Weight Atmosphere for the Super-Earth π Men c

A. García Muñoz[1], L. Fossati[2], A. Youngblood[3], N. Nettelmann[4], D. Gandolfi[5], J. Cabrera[4], and H. Rauer[1,4,6]
[1] Zentrum für Astronomie und Astrophysik, Technische Universität Berlin, Hardenbergstrasse 36, D-10623 Berlin, Germany; garciamunoz@astro.physik.tu-berlin.de, tonhingm@gmail.com
[2] Space Research Institute, Austrian Academy of Sciences, Schmiedlstrasse 6, A-8042 Graz, Austria
[3] Laboratory for Atmospheric and Space Physics, 1234 Innovation Drive, Boulder, CO 80303, USA
[4] Deutsches Zentrum für Luft- und Raumfahrt, Institut für Planetenforschung, Rutherfordstrasse 2, D-12489 Berlin, Germany
[5] Dipartimento di Fisica, Università degli Studi di Torino, via Pietro Giuria 1, I-10125, Torino, Italy
[6] Institute of Geological Sciences, Freie Universität Berlin, Malteserstrasse 74-100, D-12249 Berlin, Germany
Received 2020 October 8; revised 2020 December 16; accepted 2021 January 5; published 2021 January 29

Abstract

Strongly irradiated exoplanets develop extended atmospheres that can be utilized to probe the deeper planet layers. This connection is particularly useful in the study of small exoplanets, whose bulk atmospheres are challenging to characterize directly. Here, we report the 3.4σ detection of C II ions during a single transit of the super-Earth π Men c in front of its Sun-like host star. The transit depth and Doppler velocities are consistent with the ions filling the planet's Roche lobe and moving preferentially away from the star, an indication that they are escaping the planet. We argue that π Men c possesses a thick atmosphere with abundant heavy volatiles ($\gtrsim 50\%$ by mass of atmosphere) but that needs not be carbon rich. Our reasoning relies upon cumulative evidence from the reported C II detection, the nondetection of H I atoms in a past transit, modeling of the planet's interior, and the assumption that the atmosphere, having survived the most active phases of its Sun-like host star, will survive another 0.2–2 Gyr. Depending on the current mass of atmosphere, π Men c may still transition into a bare rocky core. Our findings confirm the hypothesized compositional diversity of small exoplanets, and represent a milestone toward understanding the planets' formation and evolution paths through the investigation of their extended atmospheres.

Unified Astronomy Thesaurus concepts: Exoplanet atmospheres (487); Exoplanet structure (495)

1. Introduction

Small exoplanets of sizes between those of Earth and Neptune are ubiquitous in the Galaxy (Batalha 2014), yet intriguingly absent in our solar system. Even when their masses and radii are accurately known (Fulton et al. 2017), little can be confidently stated about their bulk compositions (Seager et al. 2007; Rogers & Seager 2010; Valencia et al. 2010, 2013; Nettelmann et al. 2011) or the processes through which they form and evolve. The planet π Men c is a close-in transiting super-Earth (Gandolfi et al. 2018; Huang et al. 2018; mass $M_p/M_\oplus = 4.52 \pm 0.81$; radius $R_p/R_\oplus = 2.06 \pm 0.03$; orbital distance 0.06702 ± 0.00109 au) that is expected to develop an extended atmosphere under the significant X-ray and extreme ultraviolet (XUV) stellar radiation that it receives (King et al. 2019; García Muñoz et al. 2020), and therefore it is an ideal target to investigate the composition of small exoplanets. As it orbits a Sun-like star, its study also potentially conveys insight into our own solar system.

Whereas planets with radii $R_p/R_\oplus < 1.6$ are likely rocky (composed of iron and silicates) and those with $R_p/R_\oplus > 3$ are expected to have a nonnegligible amount of light volatiles (H_2/He; Otegi et al. 2020), π Men c's bulk density is consistent with an atmosphere that contains an admixture of light and heavy (e.g., H_2O, CO_2, CH_4, and NH_3) volatiles (Rogers 2015; Otegi et al. 2020), which raises the interesting possibility that it may not be H_2/He-dominated. Compositional diversity is indeed predicted by theory (Fortney et al. 2013; Mordasini et al. 2015) and supported by the scatter in the M_p–R_p statistics of known exoplanets (Hatzes & Rauer 2015; Otegi et al. 2020). Disentangling the composition of selected small exoplanets is the key next step and calls for a multiple line of evidence approach that goes beyond M_p and R_p measurements.

Transmission spectroscopy at visible–infrared wavelengths provides additional insight when gas absorption bands are revealed (Benneke & Seager 2012). However, when the measured spectrum is featureless (Guo et al. 2020), it is difficult to discriminate between atmospheres enshrouded by high-altitude clouds and atmospheres with abundant heavy volatiles. Furthermore, the precision required for visible–infrared spectroscopy approaches the limit of current and upcoming telescopes when the band-to-continuum contrast drops below ~20 parts per million (as for π Men c). Here, we instead constrain π Men c's bulk composition with far-ultraviolet (FUV) transmission spectroscopy of selected atoms in its extended atmosphere, complemented with modeling of its interior structure and atmospheric mass loss.

The manuscript is structured as follows. In Section 2, we present new FUV transmission spectroscopy measurements of π Men c and argue that the reported dimming originates in the planet's atmosphere. In Section 3, we describe our upper atmosphere modeling, with emphasis on the net mass-loss rate, the neutral/ionized state of the escaping hydrogen atoms, and their impact on atmospheric stability and the detectability of hydrogen atoms. In Section 4, we describe our planetary interior modeling, which we use to estimate the atmospheric mass for different bulk compositions. Lastly, we invoke in Section 5 an argument of stability that connects the atmospheric mass with a timescale for the planet to lose it to escape. By requiring that this timescale is not much smaller than the system's age, which would suggest fine-tuning in the evolution/current state of the planet, we are able to constrain π Men c's present-day atmospheric composition. Appendices A–D provide additional technical details.

2. Observations

We observed one FUV transit of π Men c with the Cosmic Origins Spectrograph (COS) aboard the Hubble Space Telescope (HST) over five consecutive orbits (Program: GO-15699). The first two orbits occurred before transit, the third orbit covered the ingress, and the last two orbits occurred in transit with respect to the updated ephemeris. For unknown reasons, the third observation returned no data. The data were obtained in time-tag mode with the G130M grating centered at 1291 Å. Each exposure lasted 3025 s, except the first one that was 2429 s because of target acquisition prior to the science observation. Each spectrum covers the 1135–1429 Å range, with a gap between 1274 Å and 1291 Å. For optimal stability during the observation, we adopted one single instrumental Fixed Pattern position (FP-POS = 3). We downloaded the data from MAST, and they were calibrated and extracted by calcos version 3.3.7.[7]

Each spectrum covers several stellar lines of abundant elements (i.e., hydrogen, carbon, nitrogen, oxygen, and silicon). The lines of the O I 1302–1306 Å triplet, contaminated by geocoronal airglow, were treated separately. The H I Lyα line was also severely affected by geocoronal airglow contamination (HST/COS is particularly prone to this problem) and gain sag and was not analyzed. For each of the other spectral features, we integrated the flux in wavelength to obtain a transit light curve for each line and ion. We either considered each line separately or added together the flux from different lines of the same multiplet to increase the signal-to-noise ratio (S/N; i.e., for C III, N V, C II, and Si IV). In this way, we constructed a transit light curve for each line and ion.

Among all light curves, we recorded a significant flux drop during transit only for the triplet of C II at 1334–1335 Å. This feature is composed of a resonance line at 1334.532 Å and a doublet of components at 1335.663 Å and 1335.708 Å arising from an excited state (0.007863 eV). This is why for nearby stars only the bluest line of the triplet is affected by interstellar medium (ISM) absorption (furthermore, in the nearby ISM, C II is the dominant C ion; Frisch & Slavin 2003). The C II 1335 Å doublet is unresolved with COS, and the line at 1335.663 Å is about ten times weaker than the line at 1335.708 Å, which is the strongest of the triplet. The resonance line at 1334.532 Å is intrinsically about 1.8 times weaker than the 1335.708 Å line. In our analysis we ignored the weakest component at 1335.663 Å. The light curves obtained from splitting the two main lines further indicated that the absorption signal was induced by the C II 1335 Å line (Figure 1, top). Considering only the C II 1335 Å line, the transit depth integrated across the whole line (i.e., $\pm$146 km s^{-1} from the line center) is 3.9% $\pm$ 1.1%.

We averaged the in-transit and out-of-transit data separately to obtain one master in-transit and one master out-of-transit spectrum and identify the velocities at which the absorption in the C II 1335 Å feature occurs. Figure 1 (bottom) compares the in- and out-of-transit spectra. The C II 1335 Å feature shows in-transit dimming for velocities between -70 km s^{-1} and $+10$ km s^{-1}. The corresponding transit depth over this velocity range is 6.8% $\pm$ 2.0% (3.4σ detection). The corresponding flux drop at the 1334 Å line could not be detected because of ISM absorption. We also unsuccessfully looked for absorption in this same velocity range for all of the other stellar features (Table 1).

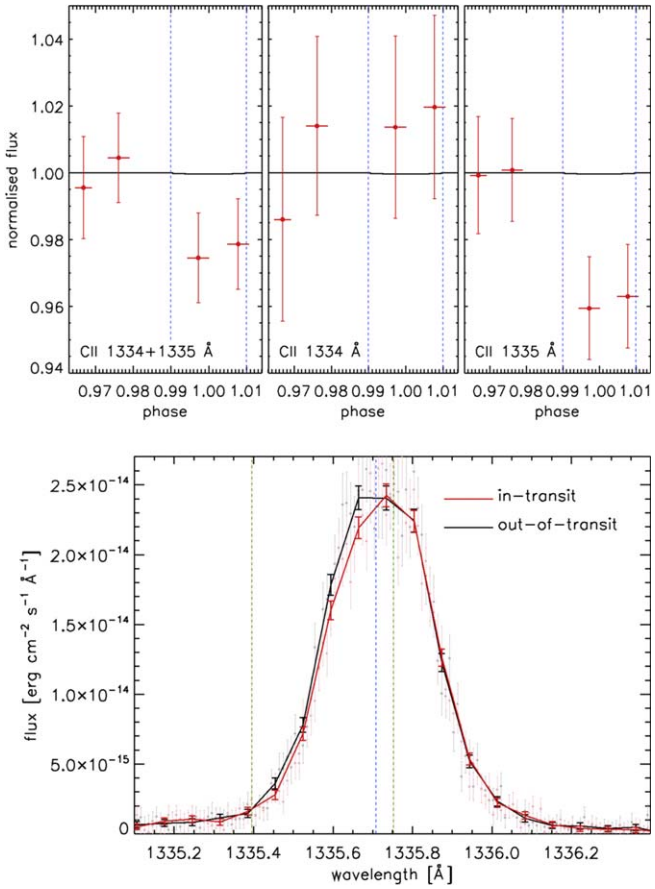

Figure 1. Top: light curves obtained from the COS spectra integrating in wavelength across the entire C II triplet at 1334–1335 Å (left), the C II 1334 Å line (middle), and the C II 1335 Å doublet (right). The horizontal bars indicate the phase range covered by each observation. Each light curve has been normalized to the average flux of the two out-of-transit points. The black line shows the optical transit light curve computed employing published system parameters (Gandolfi et al. 2018). For reference, the blue vertical dashed lines mark the phases of first and last contact. Bottom: in-transit (red) and out-of-transit (black) spectra around the position of the C II 1335 Å doublet. The spectra are rebinned every seven data points for visualization purposes and to match the instrument's spectral resolution, so that each bin corresponds to one resolution element. The gray dots show the unbinned out-of-transit spectrum. The spectra have been brought to the rest frame by accounting for the systemic velocity of the host star. The blue dashed vertical line indicates the position of the main feature composing the C II 1335 Å doublet. The green dashed–dotted vertical lines show the integration range considered for measuring the absorption.

Appendix A provides further insight into the COS data analysis and discusses the masking of the C II 1334 Å line by the ISM, the unlikeliness that the reported in-transit dimming is caused by random fluctuations in the stellar line shape, and the search for in-transit dimming at the O I 1302–1306 Å triplet. Our tests suggest that the stellar C II line does not exhibit intrinsic temporal variations and therefore that the C II 1335 Å line dimming is caused by the planet transit. Ideally, future HST/COS observations over one or more transits will confirm the above. The confirmation is obviously important for π Men c, but it is also needed to set useful precedents in the investigation of other small exoplanets with FUV transmission spectroscopy.

We attribute the dimming of the C II 1335 Å line to absorption by C II ions escaping π Men c along with other gases, even though

[7] https://www.stsci.edu/hst/instrumentation/cos/documentation/calcos-release-notes

Table 1
In-transit Absorption Measured Over the Velocity Range −70 km s^{-1} to +10 km s^{-1} for Various Stellar Emission Lines in the COS Data

Ion	Wavelength (Å)	In-transit Absorption (%)	Statistical Significance
C II	1335.7	6.76 ± 2.00	3.39
O I	1302.168	−3.65 ± 40.65	0.09
O I	1304.858	−8.33 ± 6.32	1.32
O I	1306.029	5.17 ± 3.66	1.41
Si III	1206.5	1.49 ± 2.01	0.74
N V	1238.821	−0.82 ± 5.37	0.15
N V	1242.804	−17.26 ± 9.97	1.73
Si II	1265.002	3.38 ± 4.94	0.68
Cl I	1351.656	6.12 ± 7.65	0.80
O I	1355.598	7.36 ± 5.87	1.25
Si IV	1393.755	8.41 ± 3.09	2.72
Si IV	1402.770	−0.53 ± 5.07	0.11
All ions excluding C II and O I triplet		2.67 ± 1.27	2.10

the signatures of the other gases are not directly seen in our data. Our detection adds to a growing list of exoplanets with extended atmospheres (Vidal-Madjar et al. 2003; Fossati et al. 2010; Linsky et al. 2010; Ben-Jaffel & Ballester 2013; Ehrenreich et al. 2015; Bourrier et al. 2018b). Unlike the case for π Men c, there is strong evidence that these other exoplanets' atmospheres are H_2/He-dominated. The transit depth and Doppler velocities reported here are consistent with the C II ions being swept by the stellar wind into a $\sim 15\,R_p$ wide (about the extent of the Roche lobe in the substellar direction, and closer to the planet than the interface between the planetary and stellar winds) tail and accelerated to high velocities, a scenario suggested by 3D models of π Men c and other exoplanets (Shaikhislamov et al. 2020a, 2020b). We found by means of a simplified phenomenological model of π Men c's tail (Appendix B) that the C II measurements can be explained if the planet loses carbon at a rate $\gtrsim 10^8$ g s^{-1}, requiring that the atmosphere contains this atom in at least solar abundance. A tail-like configuration facilitates the detection, but saturation of the absorption signal impedes the setting of tighter constraints on the C II abundance when it becomes supersolar. In summary, we cannot yet conclude whether carbon is a major or minor constituent of π Men c's atmosphere. Future 3D modeling that incorporates all of the relevant physics for the escaping atmosphere (including the C II ions) and its interaction with the star may help discern among atmospheric compositions with various carbon abundances.

3. Extended Atmosphere

A prior observation of π Men c with the HST Space Telescope Imaging Spectrograph (STIS) revealed no evidence for in-transit absorption of the stellar Lyα line (García Muñoz et al. 2020). When present, absorption in the Lyα wings is primarily caused by energetic neutral atoms (ENAs; Holmström et al. 2008; Tremblin & Chiang 2013), which are fast neutral hydrogen atoms generated when the low-velocity neutral hydrogen escaping the planet and the high-velocity protons in the stellar wind exchange charge:

$$\mathrm{H_{planet}\ (slow)} + \mathrm{H^{+}_{stellar\ wind}\ (fast)} \rightarrow \mathrm{H\ (fast)\ (\equiv ENA)} + \mathrm{H^{+}\ (slow)}.$$

Three-dimensional modeling shows that if π Men c's atmosphere is H_2/He-dominated, large amounts of ENAs are generated that produce measurable Lyα transit depths (Shaikhislamov et al. 2020a). Conversely, reduced ENA generation occurs if either the flux of stellar wind protons or the flux of neutral hydrogen from the planet are weak. The arrangement of C II ions into a tail suggests that the stellar wind is not weak, and therefore we disfavor the first possibility. A weak neutral hydrogen flux from the planet (the slow component of the above reaction) suggests that hydrogen is not the major atmospheric constituent or that it ionizes before interacting with the stellar wind.

We investigated π Men c's extended atmosphere and mass loss with a photochemical-hydrodynamic model (García Muñoz et al. 2020). The model takes as input the volume mixing ratio (vmr) at the 1 μbar pressure level for each species in the chemical network. Photo-/thermochemical considerations (Moses et al. 2013; Hu & Seager 2014) dictate the most abundant molecules in the bulk atmosphere given the equilibrium temperature T_{eq} and the fractions of hydrogen, helium, carbon, and oxygen nuclei (Y_{H*}, Y_{He*}, Y_{C*}, Y_{O*}; defined as the number of nuclei (symbol *) of each element divided by the total number of nuclei). For π Men c's $T_{eq} \sim 1150$ K, the bulk atmosphere composition is dominated by H_2 provided that $Y_{H*} \sim 1$. For lower Y_{H*} values, other molecules become abundant, such as H_2O, CO, CO_2, and O_2 if $Y_{C*}/Y_{O*} \ll 1$, or C_2H_2 and CO if $Y_{C*}/Y_{O*} \gg 1$. To identify the dominant gases in the bulk atmosphere for given sets of nuclei fractions and specify their vmrs at the 1 μbar pressure level, we used a published study of super-Earths and sub-Neptunes (Hu & Seager 2014; in particular their Figure 7). We considered bulk compositions in which hydrogen nuclei dominate and compositions in which carbon and oxygen nuclei are also abundant and combine into various molecules. Table 2 of Appendix C summarizes the implemented vmrs and other derived information for the battery of 30 atmospheric runs (labeled as cases 01–30) that we performed. Further details on our extended atmosphere modeling are provided in Appendix C. For the conditions explored here, the minimum and maximum loss rates are ∼1% and 3% M_p/Gyr. The loss rates depend weakly on composition even though the partitioning into different escaping nuclei can be very different.

Our models indicate that the neutral hydrogen flux (the slow component for ENA generation, see above) at a reference location defined by the sonic point is $\dot{m}_{\mathrm{H\,I}}(\mathrm{at\ Mach} = 1) \sim 5 \times 10^9$ g s^{-1} for H_2/He-dominated atmospheres. From published 3D models for H_2/He-dominated atmospheres incorporating ENAs (Holmström et al. 2008; Shaikhislamov et al. 2020a), we estimate that a neutral hydrogen flux about 1/4 times that value will bring the ENA generation in line with the nondetection of Lyα absorption. Therefore, we set $\dot{m}_{\mathrm{H\,I}}(\mathrm{at\ Mach} = 1) \lesssim 1.25 \times 10^9$ g s^{-1} as the approximate threshold for bulk compositions consistent with insufficient ENA generation and with the nondetection of Lyα absorption. Refining this approximate threshold requires the 3D modeling of π Men c's atmosphere for a diversity of bulk compositions, which should be the focus of future investigations. Although welcome, such refinements will not modify the key findings of this work.

The flux $\dot{m}_{\mathrm{H\,I}}(\mathrm{at\ Mach} = 1)$ depends strongly on the mass fraction of heavy volatiles in the atmosphere, Z (the mass of heavy volatiles relative to the mass of all volatiles), especially for $Z \gtrsim 0.4$ when hydrogen becomes preferentially ionized due to high temperatures (Figure 2; see also Figure 4 in García Muñoz et al. 2020). Remarkably, $\dot{m}_{\mathrm{H\,I}}(\mathrm{at\ Mach} = 1)$ depends weakly on the identity of the gases contributing to Z, and

Table 2
Summary of Photochemical-hydrodynamic Model Runs

Case	Y_{H^*}	Y_{C^*}	Y_{O^*}	Y_{C^*}/Y_{O^*}	Volume Mixing Ratio at $R_{1\ \mu bar}$								Z	$\dot{m}_H$(at M = 1) [10^9 g s^{-1}]	$\dot{m}_{H^*}$ [10^9 g s^{-1}]	$\dot{m}_{He^*}$ [10^9 g s^{-1}]	$\dot{m}_{C^*}$ [10^9 g s^{-1}]	$\dot{m}_{O^*}$ [10^9 g s^{-1}]	$\dot{m}$ [10^9 g s^{-1}]
					H_2	H	He	CO_2	CO	C	H_2O	O							
01	9.09(−1)	3.64(−7)	3.64(−6)	0.1	8.3(−1)	0.0	1.7(−1)	0.0	6.7(−7)	0.0	6.0(−6)	0.0	5.2(−5)	4.4	6.9	2.7	3.0(−5)	4.1(−4)	9.6
02	9.09(−1)	3.64(−6)	3.64(−5)	0.1	8.3(−1)	0.0	1.7(−1)	0.0	6.7(−6)	0.0	6.0(−5)	0.0	5.2(−4)	6.7	9.7	3.8	4.3(−4)	5.9(−3)	13.5
03	9.09(−1)	3.64(−5)	3.64(−4)	0.1	8.3(−1)	0.0	1.7(−1)	0.0	6.7(−5)	0.0	6.0(−4)	0.0	5.2(−3)	11.9	15.0	5.9	6.9(−3)	9.3(−2)	21.0
04	9.06(−1)	3.64(−4)	3.64(−3)	0.1	8.3(−1)	0.0	1.7(−1)	0.0	6.7(−4)	0.0	6.0(−3)	0.0	5.2(−2)	15.3	18.9	7.3	8.5(−2)	1.3	27.4
05†	8.73(−1)	3.64(−3)	3.64(−2)	0.1	0.0	8.8(−1)	8.8(−2)	3.7(−3)	0.0	0.0	0.0	2.9(−2)	3.7(−1)	8.4	11.5	4.5	5.9(−1)	7.5	24.1
06†	5.45(−1)	3.64(−2)	3.64(−1)	0.1	0.0	5.9(−1)	5.9(−2)	3.9(−2)	0.0	0.0	0.0	3.1(−1)	9.7(−1)	0.35	1.4	4.8(−1)	8.2(−1)	11.7	14.4
07	9.09(−1)	1.33(−6)	2.67(−6)	0.5	8.3(−1)	0.0	1.7(−1)	0.0	2.4(−6)	0.0	2.4(−6)	0.0	4.8(−5)	4.4	6.8	2.7	1.1(−4)	2.9(−4)	9.5
08	9.09(−1)	1.33(−5)	2.67(−5)	0.5	8.3(−1)	0.0	1.7(−1)	0.0	2.4(−5)	0.0	2.4(−5)	0.0	4.8(−4)	5.6	8.3	3.3	1.4(−3)	3.6(−3)	11.6
09	9.09(−1)	1.33(−4)	2.67(−4)	0.5	8.3(−1)	0.0	1.7(−1)	0.0	2.4(−4)	0.0	2.4(−4)	0.0	4.8(−3)	11.6	14.9	5.9	2.5(−2)	6.7(−2)	20.9
10	9.06(−1)	1.33(−3)	2.67(−3)	0.5	8.3(−1)	0.0	1.7(−1)	0.0	2.4(−3)	0.0	2.4(−3)	0.0	4.6(−2)	12.8	15.9	6.2	2.7(−1)	7.1(−1)	23.2
11 †	8.73(−1)	1.33(−2)	2.67(−2)	0.5	8.1(−1)	0.0	1.6(−1)	2.5(−2)	0.0	0.0	0.0	0.0	3.4(−1)	9.3	12.5	4.5	1.9	5.4	23.3
12 †	5.45(−1)	1.33(−1)	2.67(−1)	0.5	0.0	7.4(−1)	7.4(−2)	1.8(−1)	0.0	0.0	0.0	0.0	9.0(−1)	0.54	1.7	5.7(−1)	3.5	9.3	14.6
13	9.09(−1)	2.00(−6)	2.00(−6)	1	8.3(−1)	0.0	1.7(−1)	0.0	3.7(−6)	0.0	0.0	0.0	4.4(−5)	4.4	6.8	2.7	1.7(−4)	2.2(−4)	9.5
14	9.09(−1)	2.00(−5)	2.00(−5)	1	8.3(−1)	0.0	1.7(−1)	0.0	3.7(−5)	0.0	0.0	0.0	4.4(−4)	4.8	7.3	2.8	1.8(−3)	2.3(−3)	10.1
15	9.09(−1)	2.00(−4)	2.00(−4)	1	8.3(−1)	0.0	1.7(−1)	0.0	3.7(−4)	0.0	0.0	0.0	4.4(−3)	9.0	12.3	4.8	3.1(−2)	4.1(−2)	17.2
16	9.05(−1)	2.00(−3)	2.00(−3)	1	8.3(−1)	0.0	1.7(−1)	0.0	3.7(−3)	0.0	0.0	0.0	4.2(−2)	10.7	13.3	5.3	3.4(−1)	4.5(−1)	19.4
17	8.73(−1)	2.00(−2)	2.00(−2)	1	8.0(−1)	0.0	1.6(−1)	0.0	3.7(−2)	0.0	0.0	0.0	3.1(−1)	4.9	6.8	2.6	1.7	2.3	13.4
18	5.45(−1)	2.00(−1)	2.00(−1)	1	5.2(−1)	0.0	1.0(−1)	0.0	3.8(−1)	0.0	0.0	0.0	8.8(−1)	0.45	1.3	0.4	3.7	4.9	10.3
19	9.09(−1)	2.67(−6)	1.33(−6)	2	8.3(−1)	0.0	1.7(−1)	0.0	2.4(−6)	2.4(−6)	0.0	0.0	4.2(−5)	4.7	7.3	2.9	2.4(−4)	1.6(−4)	10.2
20	9.09(−1)	2.67(−5)	1.33(−5)	2	8.3(−1)	0.0	1.7(−1)	0.0	2.4(−5)	2.4(−5)	0.0	0.0	4.2(−4)	4.6	7.1	2.8	2.3(−3)	1.5(−3)	9.9
21	9.09(−1)	2.67(−4)	1.33(−4)	2	8.3(−1)	0.0	1.7(−1)	0.0	2.4(−4)	2.4(−4)	0.0	0.0	4.2(−3)	4.7	7.2	2.8	2.4(−2)	1.5(−2)	10.0
22	9.05(−1)	2.67(−3)	1.33(−3)	2	8.3(−1)	0.0	1.7(−1)	0.0	2.4(−3)	2.4(−3)	0.0	0.0	4.0(−2)	5.2	7.2	2.8	2.4(−1)	1.5(−1)	10.4
23	8.73(−1)	2.67(−2)	1.33(−2)	2	7.9(−1)	0.0	1.6(−1)	0.0	2.4(−2)	2.4(−2)	0.0	0.0	3.0(−1)	4.4	5.4	2.1	1.8	1.2	10.5
24	5.45(−1)	2.67(−1)	1.33(−1)	2	4.6(−1)	0.0	9.2(−2)	0.0	2.2(−1)	2.2(−1)	0.0	0.0	8.7(−1)	0.48	1.3	0.5	6.1	3.9	11.8
25	9.09(−1)	3.64(−6)	3.64(−7)	10	8.3(−1)	0.0	1.7(−1)	0.0	6.7(−7)	6.0(−6)	0.0	0.0	3.9(−5)	4.8	7.5	2.9	3.4(−4)	4.4(−5)	10.4
26	9.09(−1)	3.64(−5)	3.64(−6)	10	8.3(−1)	0.0	1.7(−1)	0.0	6.7(−6)	6.0(−5)	0.0	0.0	3.9(−4)	4.8	7.5	3.0	3.4(−3)	4.4(−4)	10.5
27	9.09(−1)	3.64(−4)	3.64(−5)	10	8.3(−1)	0.0	1.7(−1)	0.0	6.7(−5)	6.0(−4)	0.0	0.0	3.9(−3)	5.0	7.8	3.1	3.6(−2)	4.6(−3)	10.9
28	9.05(−1)	3.64(−3)	3.64(−4)	10	8.3(−1)	0.0	1.7(−1)	0.0	6.7(−4)	6.0(−3)	0.0	0.0	3.7(−2)	5.3	7.9	3.1	3.7(−1)	4.7(−2)	11.4
29	8.73(−1)	3.64(−2)	3.64(−3)	10	7.8(−1)	0.0	1.6(−1)	0.0	6.5(−3)	5.8(−2)	0.0	0.0	2.9(−1)	5.1	6.6	2.6	3.1	4.0(−1)	12.7
30	5.46(−1)	3.64(−1)	3.64(−2)	10	3.9(−1)	0.0	7.9(−2)	0.0	5.3(−2)	4.7(−1)	0.0	0.0	8.7(−1)	0.67	1.5	5.9(−1)	11.1	1.4	14.6

Note. Columns 2–4 quote the assumed nuclei fractions for H, C, and O in the bulk atmosphere. Columns 6–13 quote the adopted vmrs at the μbar pressure level for H_2, H, He, CO_2, CO, C, H_2O, and O, and column 14 quotes the corresponding heavy mass fraction. Column 15 quotes the mass flux of H I atoms at the location of the sonic point, which occurs for all cases within the range $r_{Mach\ =\ 1}/R_p = 3.5$–4.6. Columns 16–19 quote the mass-loss rates of H, He, C, and O nuclei, and column 20 quotes the net mass-loss rate. †: For these cases, we specified the vmrs at 1 μbar considering that molecules such as H_2, H_2O, and O_2 become photochemically unstable before reaching the μbar pressure level. We also assume that the 1 μbar pressure level occurs at the radial distance ∼2.06 $R_\oplus$ for the TESS radius of the planet. This neglects the vertical extent of the region between a few mbars and 1 μbar, a reasonable approximation for moderate atmospheric temperatures. We impose that at the 1 μbar level the temperature coincides with the planet's T_{eq} (1150 K).

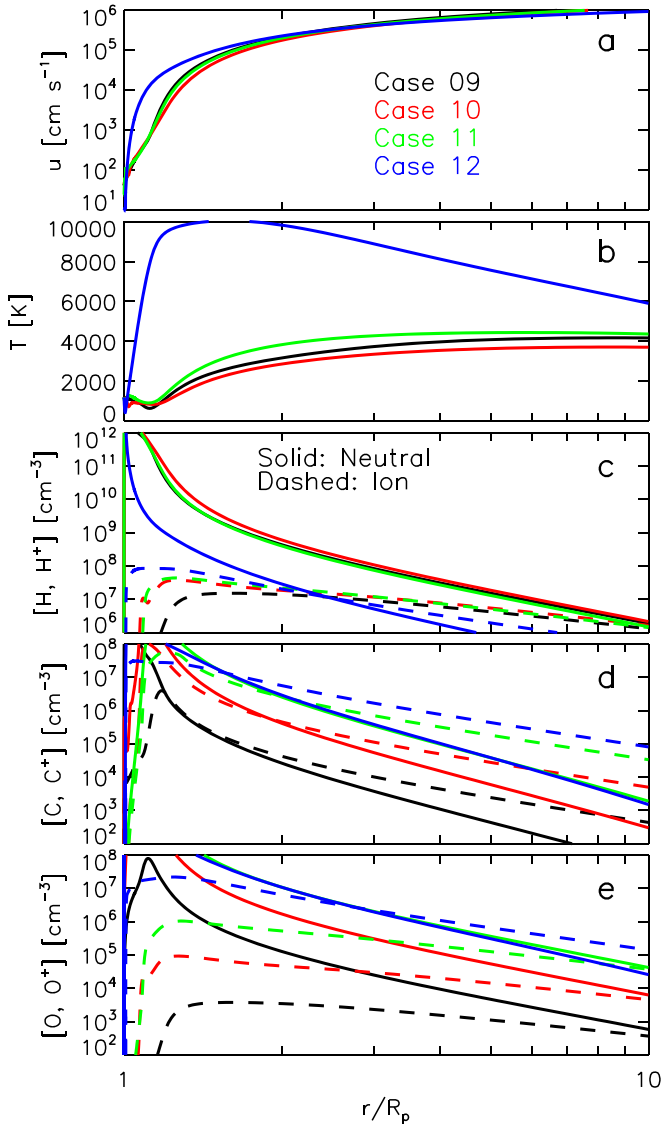

Figure 2. Photochemical-hydrodynamic solutions for selected cases from Table 2. These cases cover a broad range of heavy volatile abundances from $Z = 4.8 \times 10^{-3}$ to 0.9. (a) Velocity profiles. Most of the gas acceleration occurs below $r/R_p \sim 3$, at which location the gas reaches velocities of a few km s^{-1}. (b) Temperature profiles. Typically, the temperatures remain well below 4000–5000 K except for the higher Z, for which it reaches up to 10,000 K. This trend is seen over the entire set of 30 atmospheric runs. (c) Number density profiles for H and H$^+$. For the larger Z, the transition between these two states occurs notably closer to the planet. (d) Number density profiles for C and C$^+$. The C atom ionizes closer to the planet than do the H and O atoms. The C$^+$ photoionization lifetime is long enough ($t_{\mathrm{C\,II}} \sim 20$ hr) that it can form a long tail trailing the planet. (e) Number density profiles for O and O$^+$.

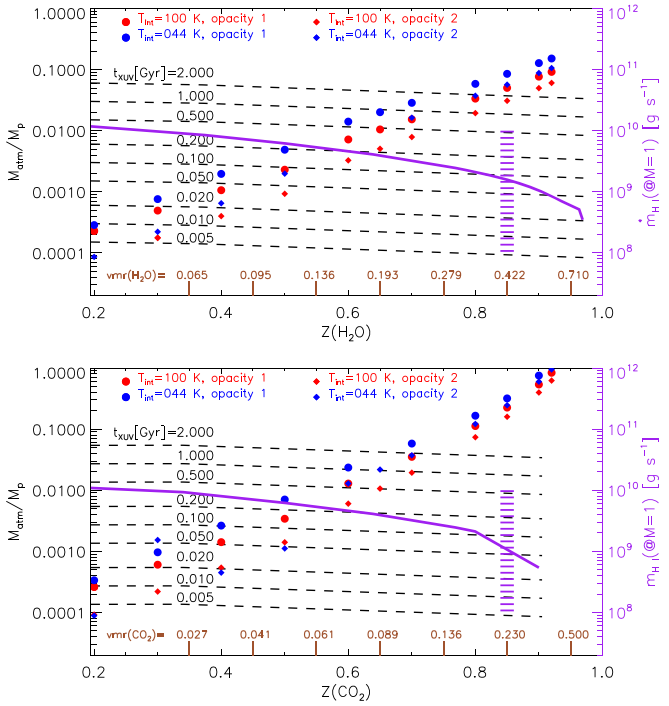

Figure 3. Atmospheric mass normalized to the measured planet mass as calculated by internal structure models for various choices of T_{int} and gas opacity. The modeling assumes H_2/He plus a heavy volatile (H_2O, top; CO_2, bottom), and explores mass fractions of heavy volatiles Z from 0.2 to about 1. For reference, the corresponding volume mixing ratio of the heavy volatile is also shown (brown). The black dashed lines show the mass fraction lost over the indicated times, from $t_{\mathrm{XUV}} = 0.005$ Gyr to 2 Gyr. For the top (bottom) panel, we used the mass-loss rates quoted in Table 2 for cases 01–06 (07–12); the choice between subsets of atmospheric runs with different Y_{C^*}/Y_{O^*} ratios is not critical though. The top panel (purple line, right axis) shows the neutral hydrogen fluxes from the planet at the sonic point predicted by the photochemical-hydrodynamic model for cases 01–06. Correspondingly, the bottom panel shows the fluxes predicted for cases 07–12. High neutral hydrogen fluxes (which occur for smaller Z) will result in enhanced ENA generation and in turn increased Lyα transit depths. The dashed purple pattern indicates our approximate threshold ($Z = 0.85$) separating atmospheric conditions that result in detectable and undetectable Lyα absorption.

indeed the calculated fluxes are comparable for each subset of atmospheric runs with different Y_{C^*}/Y_{O^*} ratios. We exploit the model-predicted Z–$\dot{m}_{\mathrm{H\,I}}$(at Mach = 1) relation (purple line in Figure 3, right axis: top panel for cases 01–06; bottom panel for cases 07–12) to infer that π Men c's atmosphere has a high Z ($\gtrsim$0.85 based on our approximate threshold for $\dot{m}_{\mathrm{H\,I}}$(at Mach = 1), although the precise Z is subject to the prescribed threshold), as otherwise the HST/STIS observation would have revealed Lyα absorption. The trend for Z–$\dot{m}_{\mathrm{H\,I}}$(at Mach = 1) in Figure 3 reflects that the partitioning between neutral and ionized hydrogen varies by a larger factor than the net mass-loss rate (which varies by $\sim$3 for the explored Z).

4. Bulk Atmosphere

We built interior structure models of π Men c that are consistent with its M_p, R_p, and T_{eq} using a tested methodology (Nettelmann et al. 2011; Poser et al. 2019). The models are organized into a rocky core of iron and silicates in terrestrial proportions, and an atmosphere on top containing H_2/He plus a single heavy volatile (CO_2 or H_2O, thus bracketing a broad range of molecular weights). This core composition produces M_p–R_p curves for atmosphereless objects consistent with the known exoplanets that presumably lack a volatile envelope (Otegi et al. 2020). When considering H_2O as the dominant heavy volatile, it is assumed that another carbon-bearing molecule present in trace amounts carries the carbon detected in the HST/COS data. We assume that all gases remain well mixed, which is justifiable for reasonable values of the eddy diffusion coefficient in the atmosphere and the mass-loss rates estimated here (García Muñoz et al. 2020). The H_2/He mass fraction is kept constant to the protosolar value, but Z is varied to explore atmospheres with different abundances of heavy volatiles. We can thus pair the interior structure models and the upper atmosphere models on the basis of their corresponding Z

and the dominating molecules (or more generally the Y_{C^*}/Y_{O^*} ratio in the upper atmosphere).

The models consider a present-day intrinsic temperature ($T_{\rm int}$, which specifies the heat flux from the interior through Stefan–Boltzmann's law $\sigma_B T_{\rm int}^4$) and an extra opacity as adjustable parameters. We find that for $T_{\rm int} > 100$ K, all plausible atmospheres are relatively light and would reach the current state within a time much shorter than the system's age (5.2 ± 1.1 Gyr) and then would continue cooling and contracting (Figure 8, top left). We consider this temperature to be a conservative upper bound. Remarkably, for all other parameters being the same, a higher $T_{\rm int}$ translates into a less massive atmosphere that is easier to lose. Indeed, increasing $T_{\rm int}$ causes larger scale heights and in turn larger atmospheric volumes for the same atmospheric mass. The best match between evolution models that include stellar irradiation as the sole external energy source and the measured $R_{\rm p}$ after cooling for 3 Gyr occurs for $T_{\rm int} = 44$–52 K (Figure 8, top left), in which case the atmosphere has reached equilibrium with the incident irradiation. In what follows, we focus on the range $T_{\rm int} = 44$–100 K. Key model outputs are the atmosphere and core masses ($M_{\rm atm}+M_{\rm core} = M_{\rm p}$) and the core radius ($R_{\rm core} \leqslant R_{\rm p}$). These quantities ($M_{\rm atm}$, $R_{\rm core}$) are determined with no prior assumption on their values by iteratively solving the interior structure equations so that upon convergence the model complies with the specified planet mass and radius constraints. For reference, the core size turns out to be always $R_{\rm core}/R_\oplus \sim 1.6$ for $Z \ll 1$, but can be $\sim$1.4 for $Z(H_2O) = 0.9$ and $\sim$1 for $Z(CO_2) = 0.9$. Appendix D provides additional insight into the interior structure model.

H_2/He-dominated atmospheres ($Z \ll 1$) are more voluminous but overall contribute little mass (Figure 3, left). For example, $M_{\rm atm}/M_{\rm p} < 2 \times 10^{-3}$ for $Z(H_2O)$ or $Z(CO_2) = 0.3$. In turn, an atmosphere with abundant heavy volatiles must be massive to compensate for its reduced scale height. Thus, $M_{\rm atm}/M_{\rm p} \sim 7 \times 10^{-2}$ for $Z(H_2O) = 0.8$, and is as high as $\sim$0.2 for $Z(CO_2) = 0.8$. However, not every atmospheric composition consistent with the interior models is stable over long timescales. We estimated the mass of atmosphere that is lost over a range of times $t_{\rm XUV}$ as $\dot{m}\ t_{\rm XUV}/M_{\rm p}$ (dashed lines, Figure 3), where $\dot{m}$ is the loss rate predicted by our photochemical-hydrodynamic models and that varies as the stellar XUV luminosity and the planet orbital distance evolve. We incorporate these effects into $t_{\rm XUV}$, which must be viewed as an equivalent time based on the current stellar luminosity and orbit.

5. Atmospheric Stability and Composition

Using arguments of atmospheric stability to constrain π Men c's interior requires an appropriate timescale over which the atmosphere will survive. We first adopted a survival time of 2 Gyr, which is a moderate fraction of the time left before the star exits the main sequence ($\sim$5 Gyr) and assumes that π Men c is not near catastrophic mass loss. This choice implicitly assumes that if the atmosphere survived the 100–1000 times enhancement in XUV luminosity experienced in the early life of its host star, then its end might not be imminent. Under this hypothesis, we infer (Figure 3) that $Z(H_2O) \geqslant 0.73$ and $Z(CO_2) \geqslant 0.65$. These are conservative bounds based on the uppermost sets of interior model curves for each heavy volatile, and correspond to volume mixing ratios $\mathrm{vmr}(H_2O) \geqslant 0.26$ (molecular weight $\mu \geqslant 6.4$ g mol^{-1}) and $\mathrm{vmr}(CO_2) \geqslant 0.09$ ($\mu \geqslant 6$ g mol^{-1}). A tenfold shorter survival time results in $Z(H_2O) \geqslant 0.50$ ($\mathrm{vmr}(H_2O) \geqslant 0.11$; $\mu \geqslant 4.1$ g mol^{-1}) and $Z(CO_2) \geqslant 0.45$ ($\mathrm{vmr}(CO_2) \geqslant 0.04$; $\mu \geqslant 4$ g mol^{-1}).

The inferred heavy mass fractions Z are approximately consistent with the nondetection of Lyα absorption, which renders independent support to our findings. It ultimately confirms that a thick atmosphere with more than half its mass in heavy volatiles is a realistic scenario for π Men c. For comparison, maximum values of $\mathrm{vmr}(H_2O) \sim 0.09$–$0.15$ have been inferred from infrared spectroscopy for the only other exoplanet with $R_{\rm p} < 3\,R_\oplus$ at which H_2O has been detected (Benneke et al. 2019; Tsiaras et al. 2019; Madhusudhan et al. 2020). Thus, π Men c becomes the exoplanet with the highest abundance of heavy volatiles known to date, and its case suggests that even higher abundances might be expected for other small exoplanets. It is uncertain how the planet acquired such a heavy atmosphere, although high-Z atmospheres are natural outcomes of formation models (Fortney et al. 2013). Assuming that water is the dominant heavy volatile, it is plausible that π Men c might have formed beyond the snow line and reached its current orbit following high-eccentricity migration and tidal circularization. The idea is supported by π Men c being on a misaligned orbit with respect to the stellar spin axis (Kunovac Hodžić et al. 2020) and the fact that the system contains a far-out gas giant on an eccentric, inclined orbit (Damasso et al. 2020; De Rosa et al. 2020; Xuan & Wyatt 2020).

Exoplanet π Men c lies near the so-called radius gap (Owen & Wu 2013; Fulton et al. 2017) that separates the population of planets that presumably lost their volatiles through atmospheric escape (peak at $R_{\rm p}/R_\oplus \sim 1.5$) from those that were able to retain them (peak at $R_{\rm p}/R_\oplus \sim 2.5$). The planet may still lose up to 10% of its mass in the future 5 Gyr if it remains on its current (and stable) orbit (De Rosa et al. 2020; Xuan & Wyatt 2020). This is more than what the planetary interior models predict for $M_{\rm atm}/M_{\rm p}$ for some plausible atmospheric configurations. It is thus likely that we are witnessing π Men c as it crosses the radius gap. Indeed, Figure 3 suggests that this will happen unless the actual $Z(H_2O) \gtrsim 0.85$ or $Z(CO_2) \gtrsim 0.80$. In that event, and because $M_{\rm atm}/M_{\rm p} \ll 1$ for such unstable configurations, the remnant core will collapse onto the empirical $M_{\rm p}$–$R_{\rm p}$ curve for atmosphereless objects.

Davide Gandolfi gratefully acknowledges financial support from the CRT foundation under grant No. 2018.2323 "Gaseous or rocky? Unveiling the nature of small worlds".

Appendix A
Preparation of the Observations and Data Analysis

We improved the published transit ephemeris (Gandolfi et al. 2018) using TESS data from Sectors 1, 4, 8, and 11–13, and the code pyaneti (Barragán et al. 2019), which allows for parameter estimation from posterior distributions.

Figure 4 shows the spectrum obtained during the second HST observation (top), marking the stellar features at which we looked for absorption in the -70 km s^{-1} to $+10$ km s^{-1} velocity range, and the resulting S/N per spectral bin (middle). The bottom panel compares the in- and out-of-transit spectra.

Having detected absorption of the C II 1335 Å feature, we looked for a similar signal at the C II 1334 Å line, without success. Next, we show that the absorption signal at 1334 Å is hidden by ISM contamination (Figure 4, bottom), which affects

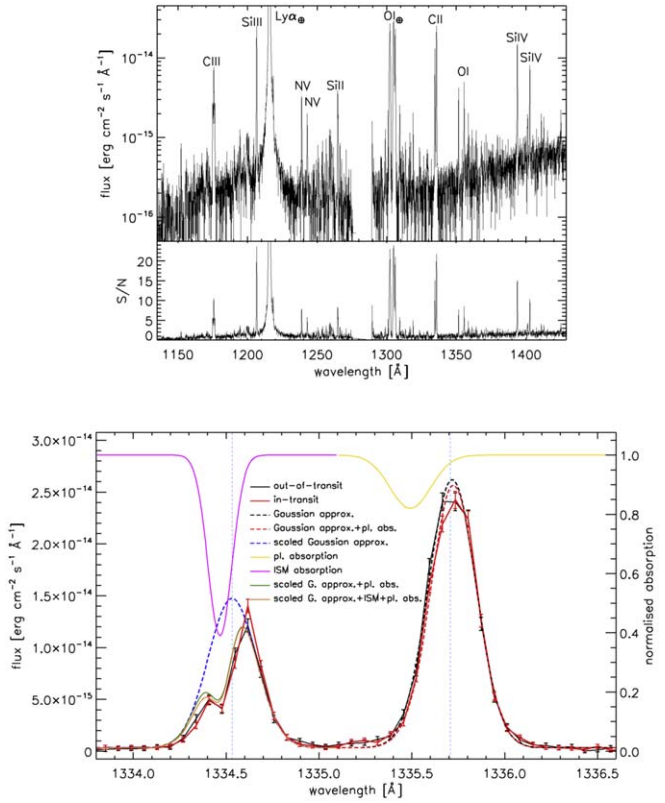

Figure 4. Top: far-ultraviolet spectrum of π Men obtained during the second HST orbit. Major features are marked. The Earth symbol indicates that the Lyα line and the O I triplet are affected by geocoronal airglow. Middle: S/N per pixel of the top panel spectrum. Bottom: rebinned out-of-transit (black) and in-transit (red) spectra of π Men around the C II 1334/1335 Å triplet. The black dashed line shows the Gaussian fit to the C II 1335 Å feature, while the blue dashed line shows the simulated C II 1334 Å line, without ISM absorption, obtained scaling the Gaussian fit to the C II 1335 Å feature by the ratio of the line oscillator strengths times the statistical weights of the lower states. The yellow line shows the fitted planetary absorption (right *y*-axis). The red dashed line shows the Gaussian fit to the C II 1335 Å feature multiplied by the simulated planetary absorption. The purple solid line shows the simulated ISM absorption (right *y*-axis), while the green solid line shows the simulated C II 1334 Å line profile multiplied by the ISM absorption profile. The orange solid line shows the C II 1334 Å line profile multiplied by the ISM and planetary absorption profiles. The vertical blue dashed lines indicate the positions of the two main components of the C II triplet.

the S/N. We first fitted the C II 1335 Å stellar feature using a Gaussian profile and the out-of-transit spectrum (black dashed line) and then employed a further Gaussian profile to fit the position and strength of the planetary absorption on the in-transit spectrum (yellow solid line). We determined that the Gaussian profile simulating the planetary absorption lies at a velocity of about -48.5 km s^{-1} with respect to the position of the main C II 1335 Å feature and has a normalized amplitude of $\sim$0.18 and a width of $\sim$0.11 Å. These fits were performed considering the unbinned spectra. We then derived the strength of the C II 1334 Å line, prior to ISM absorption, by scaling the Gaussian fit to the C II 1335 Å feature by the ratio of the oscillator strength times the statistical weight of the two lines (about 1.8; blue dashed line). We further simulated the C II ISM absorption profile at the position of the C II 1334 Å resonance line employing a Voigt profile (purple solid line), in which we set the position of the line equal to that obtained from the reconstruction of the stellar Lyα line (García Muñoz et al. 2020) and a C II ISM column density equal to that of hydrogen scaled to the expected ISM carbon-to-hydrogen abundance ratio and ISM C ionization fraction (Frisch & Slavin 2003; green solid line). Figure 4 (bottom) indicates that the simulated profile is a good match to the out-of-transit spectrum, particularly accounting for the uncertainties involved in inferring the C II ISM column density. Finally, we added to this line the planetary absorption obtained from fitting the C II 1335 Å feature, rescaled by 1.8 (orange solid line). Lastly, Figure 4 (bottom) shows that the difference between the simulated C II 1334 Å line profiles before and after adding the planetary absorption is significantly smaller than the observational uncertainties and hence undetectable in the data. In summary, reduced S/N due to ISM contamination hides the planetary absorption signal at 1334 Å.

To estimate the likelihood that our C II signal is due to intrinsic stellar variability, we did a Monte Carlo simulation where we assumed the population of intrinsic stellar variability between the mean in-transit and mean out-of-transit spectrum is represented by the measured in-transit absorption from each line (Table 1). We excluded from this representative population the C II lines because of the putative planetary absorption and the O I triplet because the noise properties and intrinsic variability of these airglow-contaminated lines are different. For the remaining eight emission lines, we calculate a weighted mean of $2.67\% \pm 1.27\%$ for the in-transit absorption. We made 10^6 realizations of nine emission lines (the eight "unaffected" lines of the representative population plus C II 1335.7 Å, the line with the 3.4σ in-transit absorption), each with in-transit absorption randomly drawn from a normal distribution with mean 2.67% and standard deviation 1.27%. We found that the likelihood of 1 or more emission lines having an absorption $\geqslant 6.76\%$ due to intrinsic stellar variability as measured by our COS spectra is 2%.

We inspected the O I lines for evidence of planetary absorption. The O I triplet at 1302–1306 Å is composed of three emission lines that share an upper energy level. O I 1302.168 Å is the resonance line and is significantly affected by ISM absorption. O I 1304.858 and 1306.029 Å each have similar oscillator strengths to the resonance line. COS's wide aperture leads to significant contamination of each line of the O I triplet by geocoronal airglow. We corrected each orbit's pipeline-reduced x1d spectrum's O I emission lines for geocoronal airglow by performing a least-squares fit of the airglow templates downloaded from MAST (Bourrier et al. 2018a) to the spectrum (Figure 5, top). We created mean in-transit and out-of-transit spectra in the same way as for the C II lines, and measured absorptions in each of the three lines (shortest wavelength to longest wavelength) of $-3.65\% \pm 40.65\%$, $-8.33\% \pm 6.32\%$, and $5.17\% \pm 3.66\%$ over the same velocity range as for C II (Figure 5, bottom). No significant variation was observed in the O I triplet. The O I line at 1355 Å similarly does not show any significant variation between in-transit and out-of-transit. Lastly, we produced time series for the flux of some stellar lines (Figure 6). The series reveals no obvious variability that could cause a false transit detection.

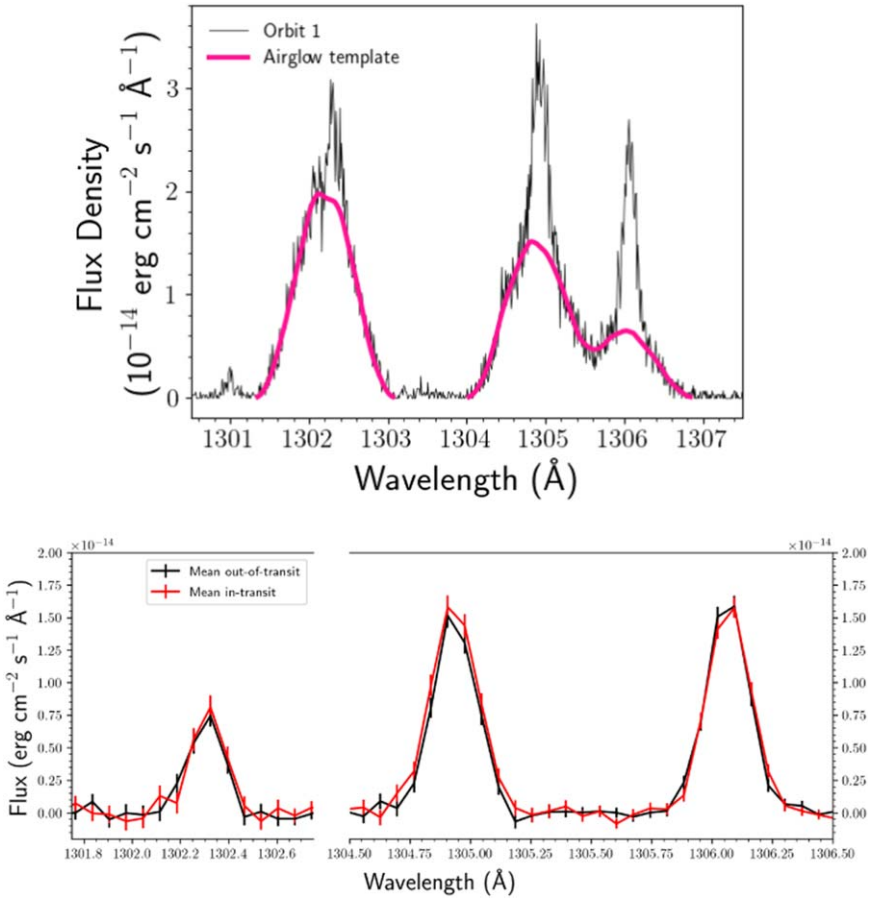

Figure 5. Top: geocoronal airglow template (Bourrier et al. 2018a) fits to Orbit 1 of our unbinned COS spectra. The narrower emission lines superimposed on the broader airglow lines have a stellar origin. These stellar lines were masked out from the fit. Orbits 2, 4, and 5 exhibit a similarly good fit. Bottom: for the O I triplet, mean in-transit (red) and mean out-of-transit (black) spectra binned in the same way as for the C II spectra after correcting for geocoronal airglow. For the line at 1306 Å (the least affected by geocoronal airglow), we estimate a transit depth of 5.2% ± 3.7% (statistically insignificant) over the velocity range from −70 km s^{-1} to +10 km s^{-1}.

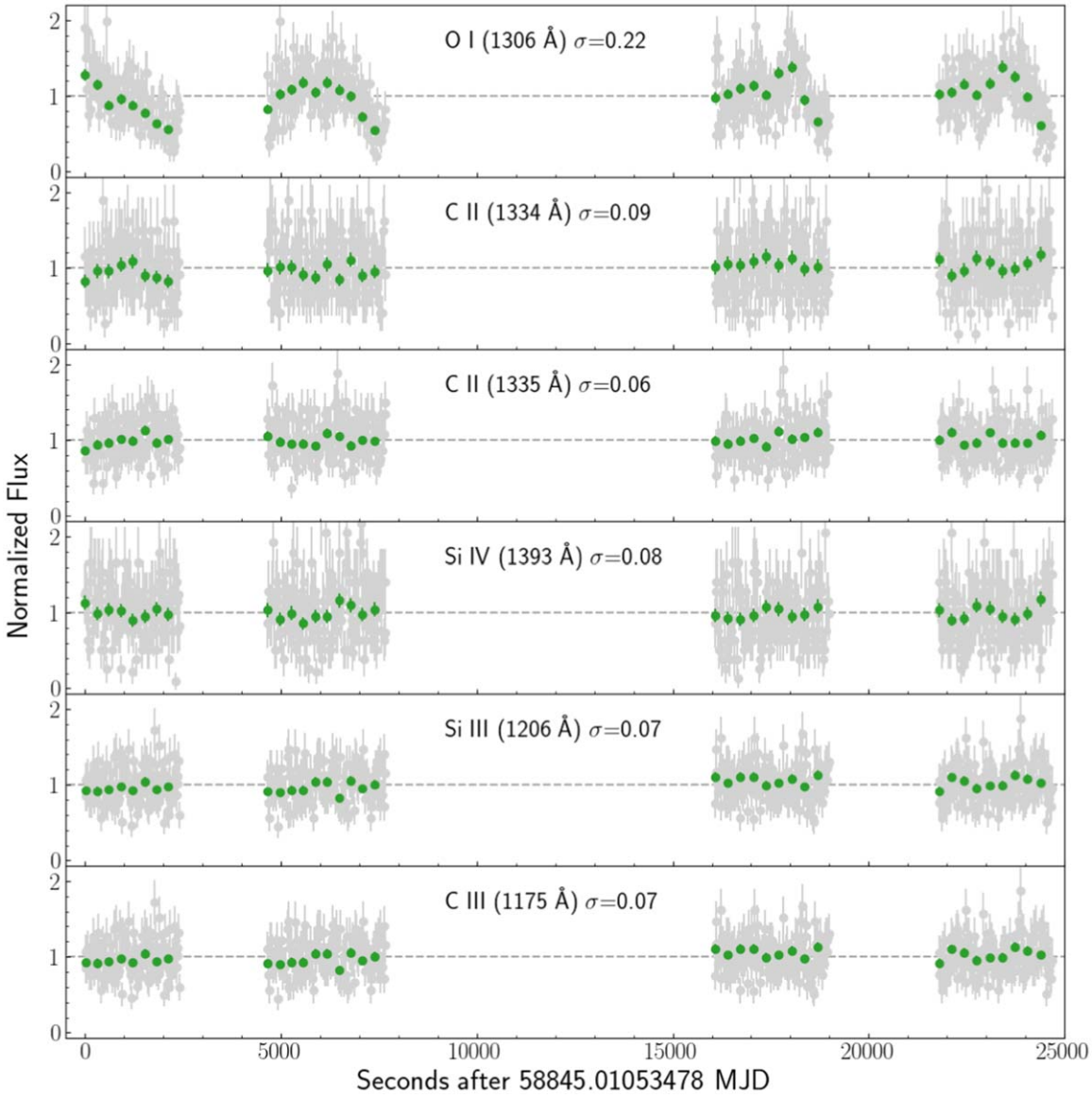

Figure 6. Normalized light curves for a selection of the observed emission lines. The gray points show 20 s bins and the green points show 300 s bins. The standard deviation of the 300 s bin points is printed in each subplot. The O I's light curve is dominated by airglow variability over the course of each orbit. No flares or other short term stellar variability are apparent.

Appendix B
Phenomenological Model of the Ion Tail

Our nominal transit depth for C II of 6.8% translates into a projected area equivalent to a disk of radius $R_{\mathrm{C\,II}}/R_{\mathrm{p}} = 15.1$. This is about the extent of π Men c's Roche lobe in the substellar direction ($R_{\mathrm{L_1}}/R_{\mathrm{p}} = 13.3$). The spectroscopic velocity of $+10\,\mathrm{km\,s^{-1}}$ for the C II ions is consistent with our photochemical-hydrodynamic predictions, and likely traces absorption in the vicinity of the planet's dayside as the gas accelerates toward the star. Comparable velocities are predicted by 3D models on the planet's dayside (Shaikhislamov et al. 2020a) before the escaping gas interacts with the impinging stellar wind. Negative velocities of $-70\,\mathrm{km\,s^{-1}}$ (and probably faster, as the stellar line becomes weak and the S/N poor at the corresponding wavelengths) suggest that the C II ions are accelerated away from the star by other mechanisms such as tidal forces and magnetohydrodynamic interactions with the stellar wind. For reference, the velocity of the solar wind at the distance of π Men c is on the order of $250\,\mathrm{km\,s^{-1}}$ (Shaikhislamov et al. 2020a). There is observational evidence for HD 209458 b, GJ 436 b and GJ 3470 b that their escaping atmospheres also result in preferential blue absorption (particularly the latter two; Vidal-Madjar et al. 2003; Ehrenreich et al. 2015; Bourrier et al. 2018b). Models considering the 3D geometry of the interacting stellar and planet winds also favor blue absorption, especially when the stellar wind is stronger (Shaikhislamov et al. 2020a, 2020b) and arranges the escaping atoms into a tail trailing the planet. We consider a C II tail to be realistic scenario for π Men c.

To gain intuition, we have built the phenomenological model of π Men c's tail sketched in Figure 7 (top). The C II ions are injected into a cylindrical tail of fixed radius $15R_{\mathrm{p}}$ and are subject to a prescribed velocity $U = -(U_0 - x/t_{\mathrm{acc}})\,\mathrm{km\,s^{-1}}$ that varies in the tail direction. This geometry surely simplifies the true morphology of the escaping gas, which is likely to resemble an opening cone tilted with respect to the star–planet line (Shaikhislamov et al. 2020a). This crude description allows us at the very least to obtain

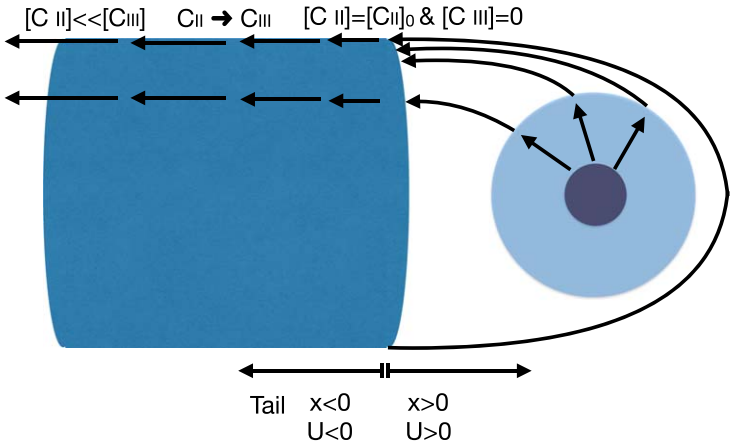

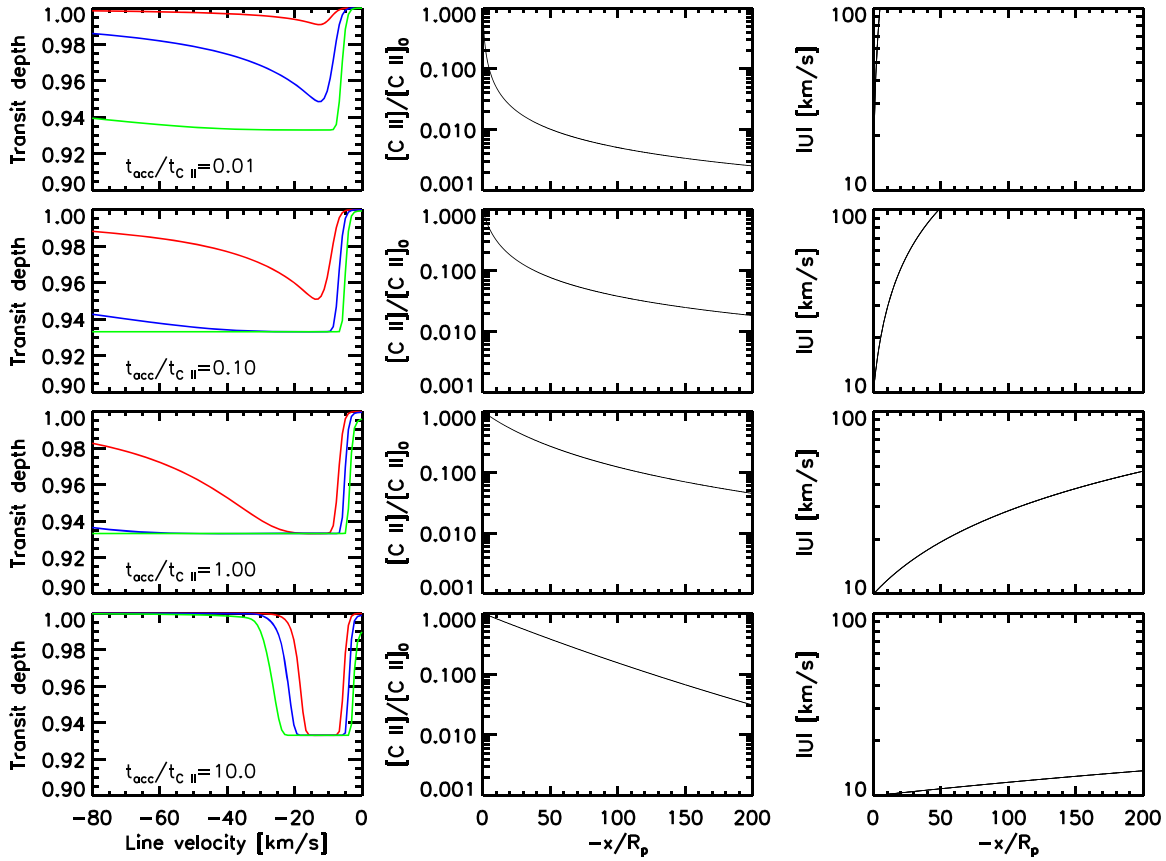

Figure 7. Top: sketch of the phenomenological model for the C II tail. The ions escaping the planet are channeled into a cylindrical tail of radius $15R_p$ and accelerated. Further ionization into C III and the gas velocity dictate the effective length of the C II tail. Both x (position from the tail entrance) and U (velocity) are negative in the tail. The star is on the right end, and the observer is on the left end. Bottom: examples of solution of the phenomenological model for acceleration-to-ionization timescales of the C II ion ranging between 0.01 and 10. Left column: transit depths for a range of C II densities at the tail entry ($x = 0$), namely, $[\text{C II}]_0 = 10^4$ (red), 10^5 (blue), and 10^6 (green) cm^{-3}. Middle column: ion number densities normalized to the density at $x = 0$. Right column: prescribed velocity profiles.

analytical expressions for some of the relevant diagnostics. Here, $U_0 = 10\,\text{km s}^{-1}$ (a typical value from the photochemical-hydrodynamic simulations; Figure 2) and t_{acc} is an acceleration timescale. (Note: $x < 0$ in the tail, and the ions are permanently accelerating.) Related accelerations have been predicted by physically motivated 3D models (Ehrenreich et al. 2015; Shaikhislamov et al. 2020a, 2020b), under the combined effect of gravitational, inertial, and radiative forces. Magnetic interactions with the stellar wind might additionally affect ion acceleration.

The C II ions photoionize further into C III with a timescale $t_{\text{C II}} \sim 20$ hr (calculated for unattenuated radiation from π Men at wavelengths shorter than the 508 Å threshold and the corresponding C II cross section; Verner & Yakovlev 1995). The collision of stellar wind particles with the planetary C II ions might ionize further the latter (ionization potential of 24 eV), especially at the mixing layer between the two flows (Tremblin & Chiang 2013), but it remains unclear whether collisional ionization can compete on the full-tail scale with

photoionization. This should be assessed in future work. The continuity equations that govern the model are:

$$\frac{d([\mathrm{C\ II}](x)U(x))}{dx} = -\frac{[\mathrm{C\ II}](x)}{t_{\mathrm{C\ II}}}$$
$$\frac{d([\mathrm{C\ III}](x)U(x))}{dx} = +\frac{[\mathrm{C\ II}](x)}{t_{\mathrm{C\ II}}}.$$

As the flow accelerates through the tail, the total density decays and the C II ions are converted into C III. The solution for the C II ion number density is:

$$\frac{[\mathrm{C\ II}](x)}{[\mathrm{C\ II}]_0} = \left(\frac{1}{1-\frac{x}{U_0 t_{\mathrm{acc}}}}\right)^{1+t_{\mathrm{acc}}/t_{\mathrm{C\ II}}}.$$

This highly simplified exercise aims to estimate reasonable values for the free parameters $[\mathrm{C\ II}]_0$ and t_{acc} that reproduce the transit depth and Doppler velocities from the COS data. To produce the wavelength-dependent opacity, we integrate $[\mathrm{C\ II}](x)$ along the line of sight keeping track of the Doppler shifts introduced by the varying $U(x)$. We represent the C II cross section at rest for the 1335.7 Å line by a Voigt line shape with thermal ($T = 6000$ K, a reference temperature in the tail; our findings do not depend sensitively on this temperature, as the absorption over a broad range of velocities is caused by the bulk velocity of the ions rather than by their thermal broadening) and natural (Einstein coefficient $A_{\mathrm{ul}} = 2.88 \times 10^8\ \mathrm{s}^{-1}$) broadening components, and a fractional population of the substate from which the line arises based on statistical weights and equal to 2/3.

Figure 7 (bottom) shows how $[\mathrm{C\ II}]_0$ and $t_{\mathrm{acc}}/t_{\mathrm{C\ II}}$ affect the absorption of the stellar line. Absorptions consistent with the measurements are generally found for $[\mathrm{C\ II}]_0 \geqslant 10^4\ \mathrm{cm}^{-3}$ and $t_{\mathrm{acc}}/t_{\mathrm{C\ II}} \leqslant 1$, and result in C II tails longer than $\sim 50 R_{\mathrm{p}}$ and large amounts of C II moving at $-70\ \mathrm{km\ s}^{-1}$. A key outcome of the model is that for $t_{\mathrm{acc}}/t_{\mathrm{C\ II}} > 1$, the C II ion photoionizes too quickly to produce significant absorption at the faster velocities. This could in principle be compensated for by increasing amounts of C II ions entering the tail, but the photochemical-hydrodynamic model indicates that it is not possible to go beyond $[\mathrm{C\ II}]_0 \sim 10^6\ \mathrm{cm}^{-3}$ without obtaining unrealistically large escape rates. For $[\mathrm{C\ II}]_0 \sim 10^4$–$10^6\ \mathrm{cm}^{-3}$, the mass fluxes of carbon atoms through the tail range from $\sim 10^8\ \mathrm{g\ s}^{-1}$ to $\sim 10^{10}\ \mathrm{g\ s}^{-1}$. These mass fluxes are comparable to the loss rates of carbon nuclei predicted by our photochemical-hydrodynamic model for atmospheres that have carbon abundances larger than solar (Table 2). This sets a weak constraint on the carbon abundance that prevents us for the time being from assessing whether carbon is a major constituent of π Men c's atmosphere.

This insight into π Men c's carbon abundance, even though of limited diagnostic value, is consistent with the interpretation of in-transit absorption by C II at the hot Jupiter HD 209458 b (Vidal-Madjar et al. 2004; Ben-Jaffel & Sona Hosseini 2010; Linsky et al. 2010). Both HD 209458 b and π Men c transit Sun-like stars and exhibit similar transit depths. Three-dimensional models of HD 209458 b (Shaikhislamov et al. 2020b) show that its C II absorption signal is explained by carbon in solar abundance. Because the predicted mass-loss rate of HD 209458 b is an order of magnitude higher than for π Men c (a result mainly from its lower density), a reasonable guess is that a ten times solar enrichment for π Men c will result in comparable transit depths. Future 3D modeling of the interaction of the C II ions with the stellar wind and the planet's magnetic field lines should help refine these conclusions.

Appendix C
Photochemical-hydrodynamic Model

We investigated π Men c's extended atmosphere with a 1D photochemical-hydrodynamic model that solves the gas equations at pressures $\leqslant 1$ μbar (García Muñoz et al. 2020). Heating occurs from absorption of stellar photons by the atmospheric neutrals. Cooling is parameterized as described in our previous work, and includes emission from H_3^+ in the infrared, Lyα in the FUV, atomic oxygen at 63 μm and 147 μm, and rotational cooling from H_2O, OH, and CO also in the infrared. We adopted an NLTE formulation of H_3^+ cooling that captures the departure of the ion's population from equilibrium at low H_2 densities. We included a parameterization of CO_2 cooling at 15 μm (Gordiets et al. 1982). The model considers 26 chemicals (H_2, H, He, CO_2, CO, C, H_2O, OH, O, O_2, H_2^+, H^+, H_3^+, He^+, HeH^+, CO_2^+, CO^+, C^+, HCO_2^+, HCO^+, H_2O^+, H_3O^+, OH^+, O^+, O_2^+, and electrons) that participate in 154 chemical processes. It does not include hydrocarbon chemistry, although this omission is not important as hydrocarbons are rapidly lost at low pressures in favor of other carbon-bearing species (Moses et al. 2013).

To explore a broad range of compositions, we adopted nuclei fractions Y_{C^*} and Y_{O^*} such that $Y_{\mathrm{C}^*}+Y_{\mathrm{O}^*}$ goes from a few times 10^{-6} to ∼0.4, and $Y_{\mathrm{C}^*}/Y_{\mathrm{O}^*}$ ratios from 0.1 to 10. We imposed $Y_{\mathrm{He}^*} = 0.1 Y_{\mathrm{H}^*}$. By definition $Y_{\mathrm{H}^*} + Y_{\mathrm{He}^*}+Y_{\mathrm{C}^*}+Y_{\mathrm{O}^*} = 1$, and therefore the composition is specified by only two nuclei fractions. With the above information, we estimated the corresponding vmrs from Figure 7 of Hu & Seager (2014) and assigned them as boundary conditions of our extended atmosphere model. For the other gases, we adopted zero vmrs. Hydrocarbons (e.g., C_2H_2, CH_4) become abundant in the bulk atmosphere for $Y_{\mathrm{C}^*}/Y_{\mathrm{O}^*} \geqslant 2$. Because our model does not currently include hydrocarbons, we transferred all of the C nuclei at the base of the extended atmosphere from C_2H_2 and CH_4 into CO and C.

Table 2 summarizes 30 cases, each for a different bulk atmospheric composition. For cases 05–06 and 11–12 we first assumed for their vmrs in the bulk atmosphere:

1. (05) H_2: 7.66×10^{-1}; He: 1.66×10^{-1}; CO: 6.90×10^{-3}; H_2O: 6.21×10^{-2}.
2. (06) He: 1.46×10^{-1}; CO_2: 9.76×10^{-2}; H_2O: 7.32×10^{-1}; O_2: 2.44×10^{-2}.
3. (11) H_2: 7.88×10^{-1}; He: 1.63×10^{-1}; CO: 2.48×10^{-2}; H_2O: 2.48×10^{-2}.
4. (12) H_2: 4.47×10^{-1}; He: 1.18×10^{-1}; CO_2: 1.45×10^{-1}; CO: 1.45×10^{-1}; H_2O: 1.45×10^{-1}.

However, our numerical experiments showed that H_2O (but also H_2 and O_2) were unstable for these cases, and their number densities dropped by orders of magnitude in a few elements of the spatial grid. This is evidence that these molecules chemically transform before reaching the μbar pressure level. To avoid numerical difficulties, in these four cases we prescribed the vmrs at the μbar pressure level by replacing the unstable molecules by their atomic constituents while preserving the original nuclei fractions. They are indicated with a † in Table 2, which lists the adopted vmrs.

The mass fraction of, e.g., H_2 and He is given by the ratio $\mathrm{vmr}(H_2)\mu_{H_2}/(\sum_s \mathrm{vmr}_s\,\mu_s)$ and $\mathrm{vmr}(\mathrm{He})\ \mu_{\mathrm{He}}/(\sum_s \mathrm{vmr}_s\ \mu_s)$, with the summation extending over all species, respectively. The mass fraction of heavy volatiles in the bulk atmosphere Z is calculated as one minus the added mass fractions of H_2 and He.

The right-hand side of Table 2 summarizes the model outputs. $\dot{m}_{\mathrm{H}}$(at Mach = 1) quotes the mass flux of neutral H I atoms at the sonic point. It departs from the mass-loss rate of H nuclei ($\dot{m}_{\mathrm{H}^*}$) if at the sonic point hydrogen is ionized. The terms $\dot{m}_{\mathrm{He}^*}$, $\dot{m}_{\mathrm{C}^*}$, $\dot{m}_{\mathrm{O}^*}$, and $\dot{m}$ quote the mass-loss rates of the specified nuclei and the net mass-loss rate of the atmosphere. All mass-loss rates are calculated over a 4π solid angle.

Table 2 shows that $\dot{m}_{\mathrm{H}}$(at Mach = 1) is about 5×10^9 g s^{-1} for an H_2/He atmosphere. Three-dimensional simulations of π Men c's extended atmosphere (Shaikhislamov et al. 2020a) show that the Lyα absorption signal varies monotonically with the mass flux of protons in the stellar wind. According to their numerical experiments (their Figure 4), increases in the stellar wind flux by a factor of a few result in deeper transits by a similar factor of a few. Because ENA generation depends on both the flux of protons in the stellar wind and the flux of neutral hydrogen in the planet wind, we estimate that a factor of a few (we take $\times1/4$) decrease in $\dot{m}_{\mathrm{H}}$(at Mach = 1) with respect to the case of an H_2/He atmosphere suffices to bring ENA generation to undetectable levels for HST/STIS. We take $\dot{m}_{\mathrm{H}}(\mathrm{at\ \ Mach}=1)=1.25\times10^9$ g s^{-1} as our approximate threshold for nondetection of Lyα absorption. A refined estimate of this threshold calls for 3D simulations over a variety of bulk atmospheric compositions.

Appendix D
Interior Structure Model

As the adopted intrinsic temperature affects the predicted atmospheric mass (because of its impact on the scale height), we constrain its possible values through thermal evolution calculations. For an adiabatic planetary envelope that cools efficiently by convection under the moderating effects of atmospheric opacity, a pattern emerges: the lower the present-day T_{int} and the more massive the atmosphere is, the longer it takes to cool down to that state from an initial hot state (T_{int} much larger than 100 K) after formation (time $t=0$).

Figure 8 (top left) shows evolution tracks for different present-day T_{int} and a heavy volatile mass fraction $Z=0.85$. The largest T_{int} that yields a cooling time in agreement with the system's age is 52 K, although $T_{\mathrm{int}}=60$ K might yield a solution where the radius is matched within the measurement uncertainties. Assuming $T_{\mathrm{int}}=100$ K requires an extra heating source that maintains such a high heat flux at present times. For inflated hot Jupiters, extra heating of ~0.1% to a few percent of the incident stellar irradiation is required to explain their large radius, which is consistent with ohmic heating (Thorngren & Fortney 2018). For π Men c, less extra heating is required (~0.01%; gray dashed curve). However, the mechanism that may provide this extra heating to the smaller π Men c is not obvious. While ohmic heating may occur at sub-Neptunes (Pu & Valencia 2017), the predicted amount falls short by two orders of magnitude of what is needed for π Men c (Figure 8, top right). Another option is tidal heating, provided that the planet is on an eccentric orbit, although the orbital eccentricity remains poorly constrained (Gandolfi et al. 2018; Huang et al. 2018; Damasso et al. 2020). For an eccentricity $e=0.001$ and tidal quality factor $Q_{\mathrm{p}}\geqslant10^3$, we find that tidal heating affects negligibly the planetary cooling. Tidal heating, however, becomes effective at extending the cooling time of an atmosphere with $T_{\mathrm{int}}=100$ K up to the current system's age if, for example, $e=0.02$ and $Q_{\mathrm{p}}\sim10^3$ (about three times the Earth's tidal quality factor), or if $e=0.1$ and $Q_{\mathrm{p}}\sim5\times10^4$ (about the Saturn/Uranus/Neptune value). Further, we estimated that the circularization time for these two configurations (Jackson et al. 2008) is $\tau_{\mathrm{circ}}=0.6$ and 30 Gyr, respectively. Even the shortest of them is on the order of our prescribed survival time. It is therefore reasonable to expect that the recent history of π Men c's atmosphere may have occurred while the planet followed an eccentric orbit that could have sustained $T_{\mathrm{int}}\sim100$ K. It is also conceivable that the outer companion in the π Men planetary system may endow a nonnegligible eccentricity to the innermost planet's orbit (De Rosa et al. 2020; Kunovac Hodžić et al. 2020; Xuan & Wyatt 2020), as is found in some close-in sub-Neptune-plus-cold Jupiter systems. Importantly, to the effects of planet mass loss, higher T_{int} values that imply lower M_{atm} are less likely to survive over timescales of gigayears, which sets a limit to how high T_{int} can be given that π Men c still hosts an atmosphere. Finally, we adopt $T_{\mathrm{int}}=100$ K as a reasonable upper limit for π Men c.

Figure 8 (bottom left) shows evolution tracks for Z from 0.5 to 0.88 at present-day $T_{\mathrm{int}}=52$ K. The lower the adopted Z, the less massive the atmosphere is and the quicker it cools down and contracts. Eventually, the planet adopts a state of (nearly) equilibrium evolution with the incident flux, where contraction slows down and further cooling progresses on very long timescales. In this state, the planet radiates ($\sim(100\ \mathrm{K}/1150\ \mathrm{K})^4\sim6\times10^{-5}$) only 0.006% more than if it were in true equilibrium with the stellar irradiation. Mass fractions $Z<0.5$ may be possible for present $T_{\mathrm{int}}<44$ K. For comparison, Saturn has $T_{\mathrm{int}}\sim77$ K and Neptune ~53 K, and therefore we do not expect that T_{int} at π Men c will be much higher than for them given that its mass is much lower. Also, a nonzero eccentricity may keep T_{int} above such values. Mass loss, fixed in the preparation of Figure 8 (bottom left) to 2×10^{10} g s^{-1}, prolongs the cooling time immediately after formation but speeds up the contraction well into the future as the planet loses its envelope.

We have simulated the future evolution of π Men c for some of the compositions deemed realistic for present-day π Men c with the goal of exploring whether the planet will ever cross the radius valley. As an example, Figure 8 (bottom right) shows that for $Z(CO_2)=0.50$ and $T_{\mathrm{int}}=44$ K, π Men c will turn into a bare rocky core in about 0.5 Gyr. The same conclusion is found for other Z–T_{int} combinations.

The interior structure model calculates the atmospheric pressure–temperature (p–T) profile using an analytical formulation (Guillot 2010) that depends on the ratio $\gamma=\kappa_{\mathrm{vis}}/\kappa_{\mathrm{IR}}$ of constant visible and IR opacities in the T–optical depth relation and on the local opacity. For the IR opacities, we took the Rosseland mean κ_{R} for solar composition (Freedman et al. 2008) as our baseline. In our opacity 1 setting, we adopted $\gamma=0.123$ and $\kappa_{\mathrm{IR}}=1\times\langle\kappa_{\mathrm{R}}\rangle$ (bracket $\langle\rangle$ denotes average over wavelength) which was confirmed to reproduce well the p–T profiles published for the H_2/He/H_2O atmosphere of K2-18 (Scheucher et al. 2020). As π Men c's atmosphere may also contain large abundances of CO_2, our opacity 2 setting adopted $\gamma=0.500$ and $\kappa_{\mathrm{IR}}=2\times\langle\kappa_{\mathrm{R}}\rangle$, which is appropriate for a CO_2-dominated atmosphere with some admixture of H_2/He. Using two sets of

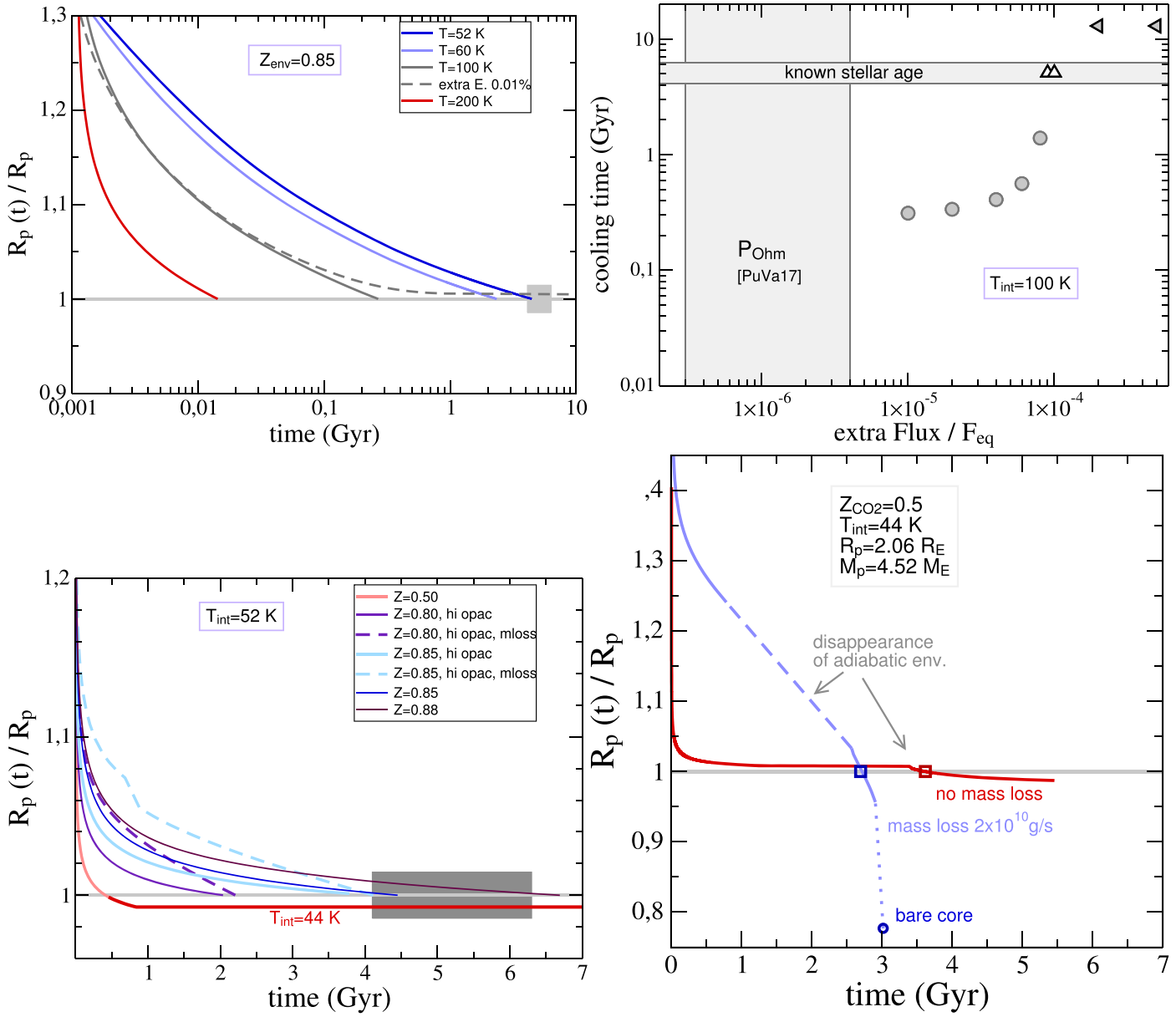

Figure 8. Top left: temporal evolution of planet radius $R_p(t)$ scaled by the measured $R_p = 2.06\,R_\oplus$ for models with $Z(CO_2) = 0.85$ and present-day T_{int} values as labeled. Both R_p and T_{int} decrease with time as the planet cools. The gray box indicates the uncertainty in present radius ($\pm 0.03\,R_\oplus$) and stellar age (5.2 ± 1.1 Gyr). For the gray dashed curve of $T_{int} = 100$ K, the evolution calculations include an extra energy source that converts 0.01% of the incident energy flux into heating of the interior. Top right: cooling time, defined as the time to reach the measured planet radius R_p. Symbols are placed at 5.1 Gyr (13 Gyr) if contraction is halted, i.e., if R_p becomes independent of time and agrees with (remains larger than) the measured R_p. All runs are for interior models with $T_{int} = 100$ K, $Z = 0.85$, and no mass loss. Bottom left: same as top left panel, but for models with a lower $T_{int} = 52$ K and Z values as labeled. The moderate $Z = 0.50$ model seems to fall short in cooling time. However, evolving that model further to $T_{int} = 44$ K leads to equilibrium evolution and $R_p(t)$ still in agreement with the measured value. Bottom right: planet size evolution considering a fiducial mass loss of 2×10^{10} g s^{-1} (blue) and omitting mass loss (red) for $Z(CO_2) = 0.5$ and $T_{int} = 44$ K. Equilibrium is reached when mass loss is omitted. When mass loss is taken into account, the planet continues shrinking as it sheds its atmosphere until it turns into a bare rocky core, which is predicted to happen within 0.5 Gyr from now. The squares indicate potential present states of π Men c, from which the evolution is calculated backward and forward in time.

opacities for each interior model calculation is a pragmatic way of bracketing the real opacity of π Men c's atmosphere. In a conservative spirit, our constraints on the planet's bulk composition from the atmospheric stability argument utilized the opacity setting that results in the lowest Z.

ORCID iDs

A. García Muñoz https://orcid.org/0000-0003-1756-4825
L. Fossati https://orcid.org/0000-0003-4426-9530
A. Youngblood https://orcid.org/0000-0002-1176-3391
N. Nettelmann https://orcid.org/0000-0002-1608-7185
D. Gandolfi https://orcid.org/0000-0001-8627-9628
J. Cabrera https://orcid.org/0000-0001-6653-5487
H. Rauer https://orcid.org/0000-0002-6510-1828

References

Barragán, O., Gandolfi, D., & Antoniciello, G. 2019, MNRAS, 482, 1017
Batalha, N. M. 2014, PNAS, 111, 12647
Ben-Jaffel, L., & Ballester, G. E. 2013, A&A, 553, A52
Ben-Jaffel, L., & Sona Hosseini, S. 2010, ApJ, 709, 1284
Benneke, B., & Seager, S. 2012, ApJ, 753, 100

Benneke, B., Wong, I., Piaulet, C., et al. 2019, ApJL, 887, L14
Bourrier, V., Ehrenreich, D., Lecavelier des Etangs, A., et al. 2018a, A&A, 615, A117
Bourrier, V., Lecavelier des Etangs, A., Ehrenreich, D., et al. 2018b, A&A, 620, A147
Damasso, M., Sozzetti, A., Lovis, C., et al. 2020, A&A, 642, A31
De Rosa, R. J., Dawson, R., & Nielsen, E. L. 2020, A&A, 640, A73
Ehrenreich, D., Bourrier, V., Wheatley, P. J., Lecavelier des Etangs, A., & Hébrard, G. 2015, Natur, 522, 459
Fortney, J. J., Mordasini, C., Nettelmann, N., et al. 2013, ApJ, 775, 80
Fossati, L., Haswell, C. A., Froning, C. S., et al. 2010, ApJL, 714, L222
Freedman, R. S., Marley, M. S., & Lodders, K. 2008, ApJS, 174, 504
Frisch, P. C., & Slavin, J. D. 2003, ApJ, 594, 844
Fulton, B. J., Petigura, E. A., Howard, A. W., et al. 2017, AJ, 154, 109
Gandolfi, D., Barragán, O., Livingston, J. H., et al. 2018, A&A Letters, 619, L10
García Muñoz, A., Youngblood, A., Fossati, L., et al. 2020, ApJL, 888, L21
Gordiets, B. F., Kulikov, Y. N., Markov, M. N., & Marov, M. Y. 1982, JGR, 87, 4504
Guillot, T. 2010, A&A, 520, A27
Guo, X., Crossfield, I. J. M., Dragomir, D., et al. 2020, AJ, 159, 239
Hatzes, A. P., & Rauer, H. 2015, ApJL, 810, L25
Holmström, M., Ekenbäck, A., Selsis, F., et al. 2008, Natur, 451, 970
Hu, R., & Seager, S. 2014, ApJ, 784, 63
Huang, C. X., Burt, J., Vanderburg, A., et al. 2018, ApJL, 868, L39
Jackson, B., Greenberg, R., & Barnes, R. 2008, ApJ, 678, 1396
King, G. W., Wheatley, P. J., Bourrier, V., & Ehrenreich, D. 2019, MNRAS, 484, L49
Kunovac Hodžić, V., Triaud, A. H. M. J., Cegla, H. M., & Chaplin, W. J. 2020, arXiv:2007.11564
Linsky, J. L., Yang, H., France, K., et al. 2010, ApJ, 717, 1291
Madhusudhan, N., Nixon, M. C., Welbanks, L., Piette, A. A. A., & Booth, R. A. 2020, ApJL, 891, L7
Mordasini, C., Mollière, P., Dittkrist, K.-M., Jin, S., & Alibert, Y. 2015, IJAsB, 14, 201
Moses, J. I., Line, M. R., Visscher, C., et al. 2013, ApJ, 777, 34
Nettelmann, N., Fortney, J. J., Kramm, U., & Redmer, R. 2011, ApJ, 733, 2
Otegi, J. F., Bouchy, F., & Helled, R. 2020, A&A, 634, A43
Owen, J. E., & Wu, Y. 2013, ApJ, 775, 105
Poser, A. J., Nettelmann, N., & Redmer, R. 2019, Atmos, 10, 664
Pu, B., & Valencia, D. 2017, ApJ, 846, 47
Rogers, L. A. 2015, ApJ, 801, 41
Rogers, L. A., & Seager, S. 2010, ApJ, 716, 1208
Scheucher, M., Wunderlich, F., Grenfell, J. L., et al. 2020, ApJ, 898, 44
Seager, S., Kuchner, M., Hier-Majumder, C. A., & Militzer, B. 2007, ApJ, 669, 1279
Shaikhislamov, I. F., Fossati, L., Khodachenko, M. L., et al. 2020a, A&A, 639, A109
Shaikhislamov, I. F., Khodachenko, M. L., Lammer, H., et al. 2020b, MNRAS, 491, 3435
Thorngren, D. P., & Fortney, J. J. 2018, AJ, 155, 214
Tremblin, P., & Chiang, E. 2013, MNRAS, 428, 2565
Tsiaras, A., Waldmann, I. P., Tinetti, G., Tennyson, J., & Yurchenko, S. N. 2019, NatAs, 3, 1086
Valencia, D., Guillot, T., Parmentier, V., & Freedman, R. S. 2013, ApJ, 775, 10
Valencia, D., Ikoma, M., Guillot, T., & Nettelmann, N. 2010, A&A, 516, A20
Verner, D. A., & Yakovlev, D. G. 1995, A&AS, 109, 125
Vidal-Madjar, A., Désert, J.-M., Lecavelier des Etangs, A., et al. 2004, ApJL, 604, L69
Vidal-Madjar, A., Lecavelier des Etangs, A., des Désert, J.-M., et al. 2003, Natur, 422, 143
Xuan, J. W., & Wyatt, M. C. 2020, MNRAS, 497, 2096